energies

MDPI

Article

Equation of State for Bismuth at High Energy Densities

Konstantin V. Khishchenko [1,2,3,4]

[1] Joint Institute for High Temperatures of the Russian Academy of Sciences, Izhorskaya 13 Bldg 2, 125412 Moscow, Russia; konst@ihed.ras.ru
[2] Landau Phystech School of Physics and Research, Moscow Institute of Physics and Technology, Institutskiy Pereulok 9, 141701 Dolgoprudny, Moscow Region, Russia
[3] Department of Computational Mechanics, South Ural State University, Prospekt Lenina 76, 454080 Chelyabinsk, Russia
[4] Federal Research Center of Problems of Chemical Physics and Medicinal Chemistry of the Russian Academy of Sciences, Prospekt Akademika Semenova 1, 142432 Chernogolovka, Moscow Region, Russia

Abstract: The purpose of this work is to describe the thermodynamic properties of bismuth in a broad scope of mechanical and thermal effects. A model of the equation of state in a closed form of the functional relationship between pressure, specific volume, and specific internal energy is developed. A new expression is proposed for the internal energy of a zero-temperature isotherm in a wide range of compression ratios, which has asymptotics to the Thomas–Fermi model with corrections. Based on the new model, an equation of state for bismuth in the region of body-centered cubic solid and liquid phases is constructed. The results of calculating the thermodynamic characteristics of these condensed phases with the new EOS are compared with the available experimental data for this metal in waves of shock compression and isentropic expansion. The parameters of shock waves in air obtained earlier by unloading shock-compressed bismuth samples are reconsidered. The newly developed equation of state can be used in modeling various processes in this material at high energy densities.

Keywords: equation of state; bismuth; shock wave; isentropic release wave; supersonic flow in air; high energy densities

Citation: Khishchenko, K.V. Equation of State for Bismuth at High Energy Densities. *Energies* **2022**, *15*, 7067. https://doi.org/10.3390/en15197067

Academic Editor: Tatiana Lapushkina

Received: 22 August 2022
Accepted: 20 September 2022
Published: 26 September 2022

1. Introduction

Knowledge of the thermodynamic properties of materials in a wide range of high-energy states is required for the analysis of physical phenomena in various processes under intense pulse action on condensed matter [1–3]. These processes include high-velocity impact [4–7], interaction with the material of intense laser radiation [8–11] or particle flows of high power density [12–14], and the electrical explosion of conductors [15–17]. For numerical simulations of emerging hydrodynamic flows, it is necessary to know the relationships of the thermodynamic characteristics of the medium in the entire range of realizable states [18–22]. Interest in thermodynamic models is also associated, in particular, with the problems of studying the thermoelastic properties of various materials at high pressures [23–26].

Bismuth is used in nuclear power technology as a component in liquid metal coolants or solvents for fuel in nuclear reactors [27], as well as a target for charged particle beam irradiation in an accelerator-driven nuclear waste transmutation system [28–31]. In this regard, the equation of state (EOS) for bismuth in a wide range of changes in specific volume (V) and specific internal energy (E) is of interest for solving problems related to the numerical simulation of the dynamics of flows in the liquid phase and dense plasma.

In this paper, a model of the EOS for matter in the form of a function of pressure $P = P(V, E)$ is developed. In contrast to the previously known EOSs (for bismuth) [32–41], a new expression is proposed for the internal energy of matter on the zero-temperature isotherm (cold curve) in a wide range of densities ($\rho = V^{-1}$), which has asymptotics to

the Thomas–Fermi model with quantum and exchange corrections [42–45]. A new EOS is developed for a body-centered cubic (bcc) solid phase and a melt of bismuth in the high-pressure region. The results of the calculations of the shock adiabats for samples of different initial densities and release isentropes for shock-compressed samples using the new EOS are compared with the available experimental data for bismuth. In addition, the relationship between the parameters of plane shock waves in the metal and in the air adjacent to it when the front of the first wave reaches the sample–gas interface is reconsidered.

2. EOS Model

The general form of the dependence of pressure on specific volume and internal energy is chosen on the basis of the quasi-harmonic approximation:

$$P(V,E) = P_c(V) + \frac{\Gamma(V,E)}{V}[E - E_c(V)], \tag{1}$$

where E_c is the specific cold energy, i.e., specific internal energy at zero temperature, $T = 0$; and P_c is the cold pressure, i.e., pressure at $T = 0$, that is, $P_c = -\mathrm{d}E_c/\mathrm{d}V$. The coefficient Γ is the ratio of thermal pressure to thermal energy density, $\Gamma = (P - P_c)V/(E - E_c)$.

The cold energy under compression ($\varsigma = V_{0c}/V \geqslant 1$; V_{0c} is the specific volume at $T = 0$ and $P = 0$) is proposed in the following form:

$$E_c(V) = \frac{9}{2}V_{0c}B_{0c}\varsigma^{2/3}\zeta^2 \exp[K(\zeta)]. \tag{2}$$

Here, B_{0c} is the cold bulk modulus $B_c = -V\mathrm{d}P_c/\mathrm{d}V$ at $\varsigma = 1$; $\zeta = 1 - \varsigma^{-1/3}$;

$$K(\zeta) = \sum_{k=1}^{N_k} a_k \zeta^k. \tag{3}$$

The form of Equation (2) ensures that the following conditions are met:

$$E_c(V_{0c}) = 0, \tag{4}$$

$$P_c(V_{0c}) = 0, \tag{5}$$

$$B_c(V_{0c}) = B_{0c}. \tag{6}$$

The fulfillment of the condition for the value of the cold bulk modulus with respect to cold pressure $B'_c = \mathrm{d}B_c/\mathrm{d}P_c$ at $\varsigma = 1$ is required:

$$B'_c(V_{0c}) = B'_{0c}, \tag{7}$$

which gives $a_1 = B'_{0c} - 3$. In the high-density limit $\varsigma \to \infty$, $\zeta \to 0$, an asymptotic pressure behavior

$$P_c(V) \approx b_2\varsigma^{5/3} + b_1\varsigma^{4/3} \tag{8}$$

is needed, where the coefficients b_2 and b_1 are determined from consideration of the Thomas–Fermi model with quantum and exchange corrections [42–46]:

$$b_2 = \frac{3^{2/3}\pi^{4/3}Z^{5/3}}{5}\frac{a_B^2 E_H}{[Am_u V_{0c}]^{5/3}}, \tag{9}$$

$$b_1 = -\left(\frac{3^{2/3}\pi^{1/3}Z^2}{2^{1/3}5} + \frac{11Z^{4/3}}{2^2 3^{5/3}\pi^{1/3}}\right)\frac{a_B E_H}{[Am_u V_{0c}]^{4/3}}, \tag{10}$$

where a_B is the Bohr radius; E_H is the Hartree energy; m_u is the unified atomic mass unit (u); A it the atomic mass in u; and Z is the atomic number. Equation (8) gives two conditions for the coefficients a_k in Equation (3):

$$\sum_{k=1}^{N_k} a_k = \ln \frac{b_2}{3B_{0c}}, \tag{11}$$

$$\sum_{k=1}^{N_k} k a_k = -\frac{2b_1}{b_2} - 2. \tag{12}$$

The cold energy of matter in the expansion region ($\varsigma < 1$) is taken as the sum of the power functions:

$$E_c(V) = V_{0c}B_{0c}\left(\frac{a_m}{m}\varsigma^m + \frac{a_n}{n}\varsigma^n - \frac{a_m + a_n}{l}\varsigma^l\right) + E_s, \tag{13}$$

which provides the value of the sublimation energy E_s in the limit of zero density $\varsigma \to 0$ as well as the condition of Equation (5). Satisfying Equations (4), (6), and (7) leaves only two free parameters m and n in Equation (13).

In Equation (1), the coefficient Γ depends on the volume and internal energy [46]:

$$\Gamma(V, E) = \gamma_i + \frac{\gamma_c(V) - \gamma_i}{1 + \sigma^{-2/3}[E - E_c(V)]/E_a}, \tag{14}$$

where $\sigma = V_0/V$; V_0 is the specific volume under normal conditions, $E = E_0$ and $P = P_0$; γ_c is the Grüneisen coefficient $\gamma = V(\partial P/\partial E)_V$ at $T = 0$; γ_i is the value of the Grüneisen coefficient in the case of high thermal energies, $E - E_c \gg E_a\sigma^{2/3}$; and E_a is a parameter. The coefficient γ_c is represented by the volume function [47,48]

$$\gamma_c(V) = 2/3 + (\gamma_{c0} - 2/3)\frac{\delta_n + \ln^2 \sigma_m}{\delta_n + \ln^2(\sigma/\sigma_m)}, \tag{15}$$

where the value of γ_{c0} corresponds to the normal volume V_0; and σ_m and δ_n are parameters. The chosen forms of Equations (1), (14), and (15) provide the following relation:

$$\gamma_{c0} = \gamma_i + (\gamma_0 - \gamma_i)\left[1 + \frac{E_0 - E_c(V_0)}{E_a}\right]^2, \tag{16}$$

where γ_0 is the Grüneisen coefficient under normal conditions, $\gamma(V_0, E_0) = \gamma_0$.

3. Thermodynamic Properties of Bismuth

At atmospheric pressure, crystalline bismuth has a rhombohedral structure and melts at 544.5 K [49]. Under compression at room temperature, the rhombohedral structure transforms into a monoclinic structure at 2.55 GPa [50], which, in turn, transforms into an incommensurate host–guest structure of two nested body-centered tetragonal cells at 2.7 GPa [51,52]. A further increase in pressure leads to a transition to a phase with a bcc structure at 7.67 ± 0.18 GPa [50–52], which is observed up to the maximum pressure of 222 GPa reached under static conditions [53,54].

In the present work, the EOS was constructed for the region of the bcc-solid and liquid phases of bismuth. The coefficients of Equations (1)–(16), which optimally generalize the information available at high pressures and high thermal internal energies, are obtained as follows: $V_0 = 0.087$ cm^3/g, $V_{0c} = 0.086139$ cm^3/g, $B_{0c} = 55.277026$ GPa, $a_1 = 2.48$, $a_2 = 0.826667$, $a_3 = -3.051687$, $a_4 = 4.092720$, $a_m = -0.662946$, $a_n = -0.000316$, $m = 1$, $n = 12$, $l = 2.512935$, $E_s = 1.9$ kJ/g, $\gamma_{c0} = 2.3$, $\sigma_m = 1.3$, $\delta_n = 4$, $\gamma_i = 0.4$, and $E_a = 2.3$ kJ/g.

The calculated cold compression curve is presented in Figure 1. As can be seen in Figure 1, the calculated zero-temperature isotherm is in good agreement with the available

experimental data [53,54] on the compression of the bcc phase of bismuth at room temperature at pressures up to 222 GPa. In addition, the obtained dependence of pressure at $T = 0$ on the density at compression ratios above 20 agrees well with the results of calculations by Kalitkin and Kuzmina [45] using the Thomas–Fermi model with corrections [44]. The previously known cold-curve approximation [34,39] deviates noticeably from the results of pressure calculations using the Thomas–Fermi model with corrections at compression ratios above 500. The cold compression curves of the bcc phase of bismuth from the EOSs [38,40] are in good agreement with the experimental data [53,54], but they deviate greatly from the results of calculations using the Thomas–Fermi model with corrections in the range of applicability of the latter (at compression ratios above 50).

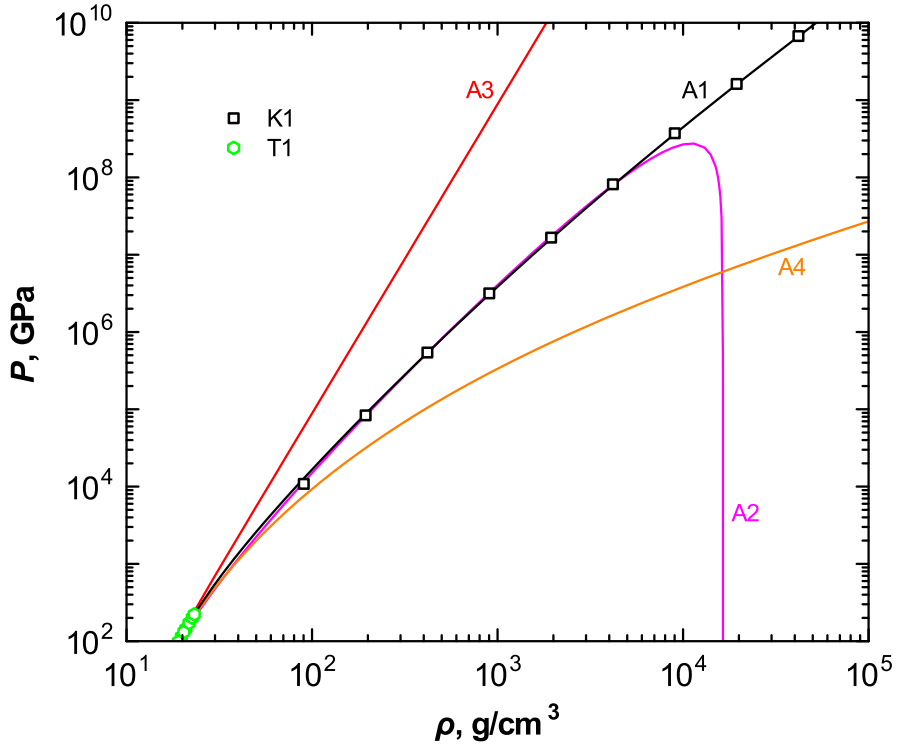

Figure 1. Pressure on the isotherm $T = 0$ as a function of density: A1—calculation results according to the present model; A2—approximation [34,39]; A3—approximation [40]; A4—approximation [38]; K1—results of calculations using the Thomas–Fermi model with corrections [44,45]; T1—experimental data at room temperature [53,54].

The shock compressibility of bismuth has been studied using traditional planar explosive systems [55–68] up to a pressure of 177 GPa. The use of hemispherical explosive systems [69,70] made it possible to obtain a pressure behind the shock wave front in this metal up to 385 GPa [56,61]. Higher shock-compression pressures in bismuth up to 675 GPa have been achieved using layered cumulative systems and cone-converging shock-wave generators [61]. A high-power laser [67] and a light-gas gun [68] were also used to study phase transformations of bismuth in shock waves.

The parameters of the shock adiabat of samples with an initial density ρ_{00} at a given pressure P are calculated by solving a system consisting of the EOS $P = P\,(V, E)$ (1)–(16) and the Rankine–Hugoniot relation [1] expressing the energy conservation law:

$$E = E_0 + \frac{1}{2}(P + P_0)(V_{00} - V), \tag{17}$$

where P_0, V_{00}, and E_0 are the pressure, specific volume, and internal energy of the matter ahead of the shock-wave front; $V_{00} = \rho_{00}^{-1}$; and P, V, and E are the pressure, specific volume, and internal energy of the shock-compressed matter behind the shock-wave front.

The velocities of the front of the shock wave and particles behind the front are found from the Rankine–Hugoniot relations [1], which express the laws of conservation of mass and momentum:

$$U_s = V_{00}\sqrt{\frac{P - P_0}{V_{00} - V}}, \tag{18}$$

$$U_p = \sqrt{(P - P_0)(V_{00} - V)}. \tag{19}$$

The results of the calculation of the shock adiabats for bismuth samples of different initial densities are shown in Figures 2–4 in comparison with the available shock-wave data [55–62,64–67]. An analysis of the figures allows one to conclude that the calculated shock adiabats are in good agreement with the experimental data in the entire studied region of states of the bcc and liquid phases of bismuth.

In experiments [61], in addition to the parameters of the shock wave in the sample, the velocity of the shock wave in the barrier (anvil) located directly behind the sample was also measured. From the known shock adiabat of the barrier material, the particle velocity and the pressure behind the front of this shock wave in the barrier can be determined. The particle velocity and pressure also correspond to the state of the sample after expanding isentropically into the barrier (if the barrier material has a dynamic impedance less than that of the sample material). Such experiments on isentropic expansion of shock-compressed samples make it possible to study a wide range of states from highly-compressed and heated condensed matter to rarefied gas and plasma.

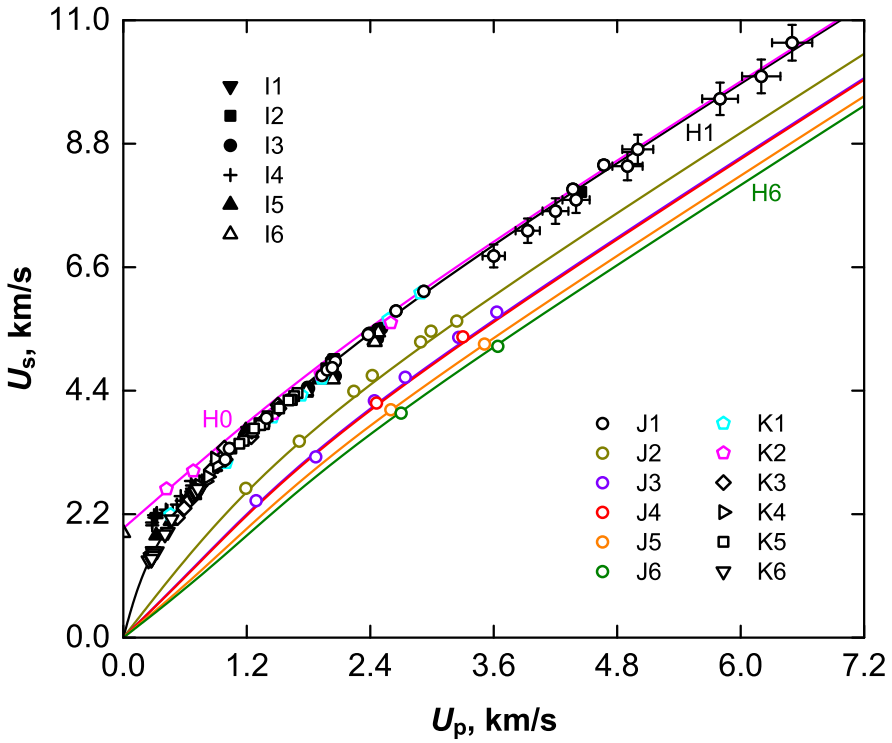

Figure 2. Shock adiabats of bismuth samples with different initial densities (ρ_{00}) and initial temperatures (T_0) at an initial normal pressure (P_0 = 0.1 MPa): solid lines—results of calculations using the present model (curve H0 corresponds to the initial state of the liquid phase at T_0 = 673 K and ρ_{00} = 9.89 g/cm^3; curves H1 to H6 correspond to the initial state of the solid phase at room temperature and ρ_{00} = 9.8, 6.62, 5.1, 5, 4 and 3.44 g/cm^3); markers—experimental data (I1—[55]; I2—[56]; I3—[57]; I4—[58]; I5—[59]; I6—[60]; J1 to J6—[61], ρ_{00} = 9.8, 6.62, 5.1, 5, 4 and 3.44 g/cm^3, respectively; K1—[62], T_0 = 88 K, solid; K2—[62], T_0 = 673 K, liquid; K3—[64]; K4—[65]; K5—[66]; K6—[67]).

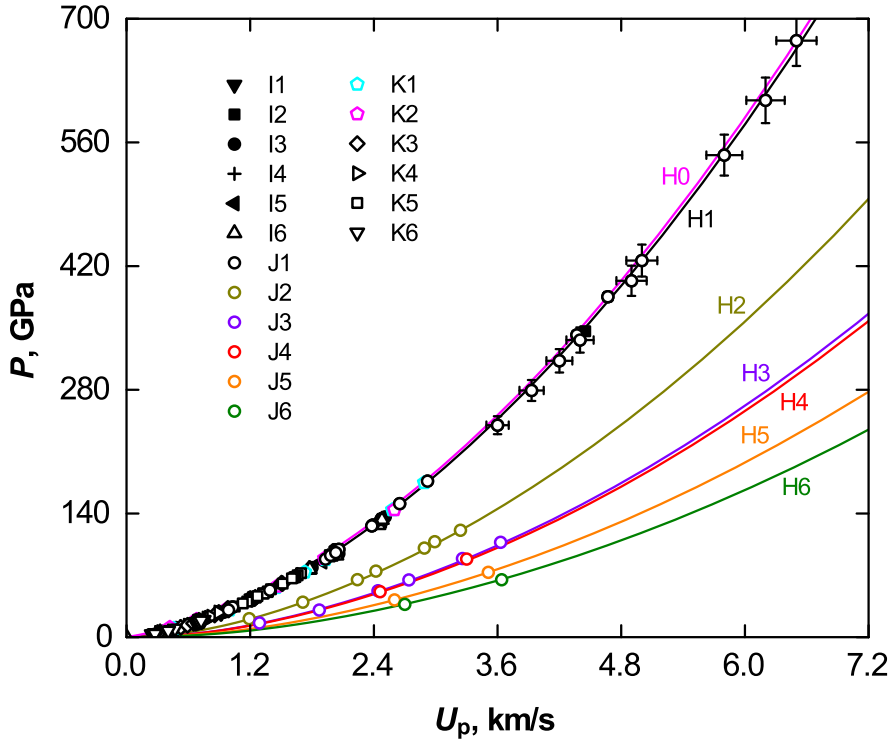

Figure 3. Shock adiabats of bismuth samples of different initial densities and initial temperatures at an initial normal pressure; designations are the same as in Figure 2.

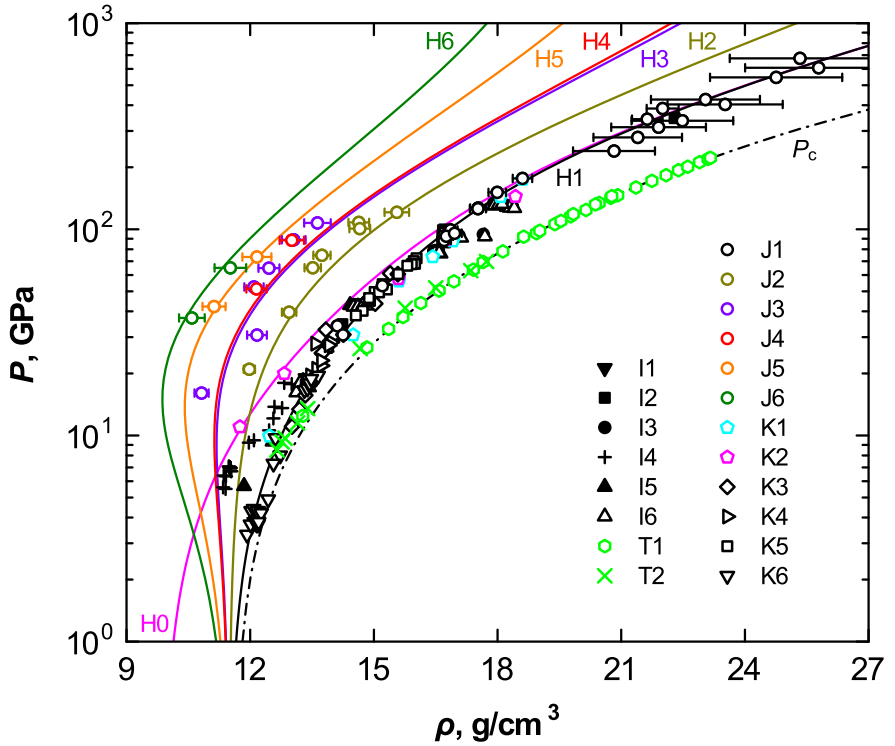

Figure 4. Diagram of states of bismuth under cold compression (P_c) and shock loading of samples of different initial densities and initial temperatures at an initial normal pressure (H0 to H6): T1 and T2—data from static experiments at high pressure and room temperature for the bcc phase (T1—[53,54]; T2—[51,52]); the rest of the designations are the same as in Figure 2.

The calculated isentropes of the unloading of shock-compressed bismuth samples of different initial densities are shown in Figure 5 along with the experimental data [61]. As can be seen, the proposed EOS is in good agreement with these data in the entire region of the achieved kinematic and dynamic parameters of the unloading waves, except for the region of the relatively low expansion velocities and pressures. According to the calculations made using another EOS model [33,34,39], which is thermodynamically complete and takes into account phase transitions, in this region of the thermodynamic parameters, bismuth melts and evaporates in isentropic expansion waves. Accounting for these effects is beyond the scope of the presented simple thermodynamically incomplete EOS model.

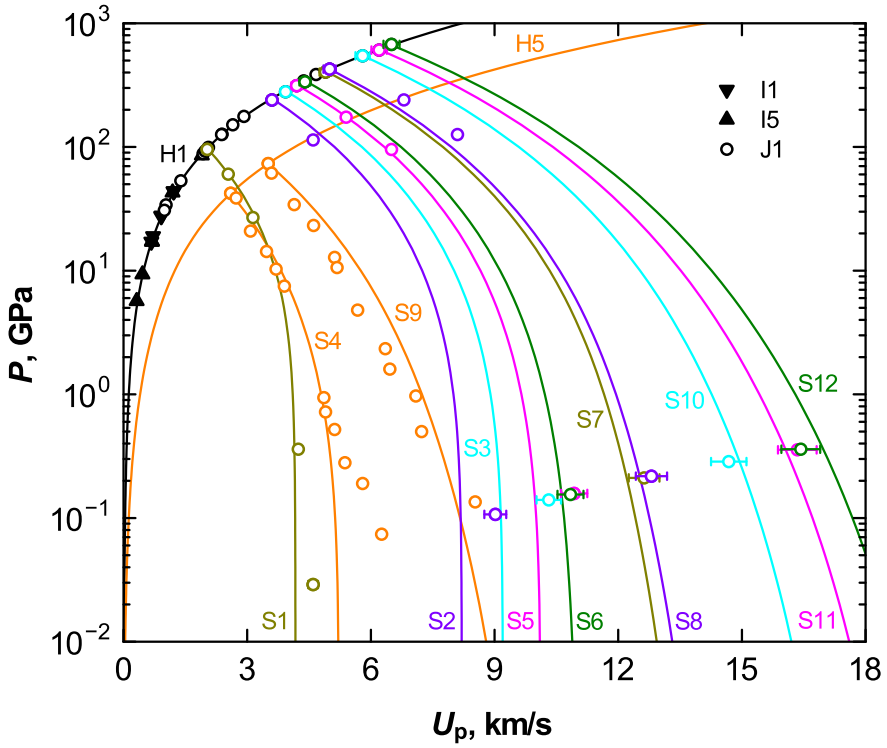

Figure 5. Shock adiabats (H1 and H5) and isentropes of unloading of the shock-compressed bismuth samples of different initial densities (S1 to S12): solid lines—results of calculations using the present model (shock adiabats H1 and H5 correspond to the initial density of the solid and porous samples $\rho_{00} = 9.8$ and 4 g/cm^3); markers—experimental data (I1—[55]; I5—[59]; J1—[61]).

In experiments [61] upon unloading shock-compressed bismuth samples into air with an initial normal pressure, the measured parameter was the velocity of the shock wave in air, which was pushed by the free surface of the shock-compressed sample. In experiments [55,59], the velocity of the free surface of the sample (i.e., the interface with air) was taken as the measured parameter of the supersonic flow in air. The shock velocity (for the experiments in [55,59]) or particle velocity (for the experiments in [61]) and pressure in shock-compressed air can be determined from the known shock adiabat of this gas [71]. The results of such a calculation are presented in Figures 5–7 and Table 1. The initial densities of the bismuth samples are taken as $\rho_{00} = 9.79$ g/cm^3 for the case in [55], 9.776 g/cm^3 for [59], and 9.8 g/cm^3 for [61]; the initial density of air is taken as $\rho_{00\,\mathrm{air}} = 1.2040$ mg/cm^3 [71] for all three cases; $P_0 = 0.1$ MPa. It should be noted that the values of pressure and particle velocity determined with the use of experimental data [61] in this work differ somewhat from those given in [61]. Apparently, this can be explained by the difference in the parameters of the shock adiabat and the initial density of air taken in [61] and in the present work.

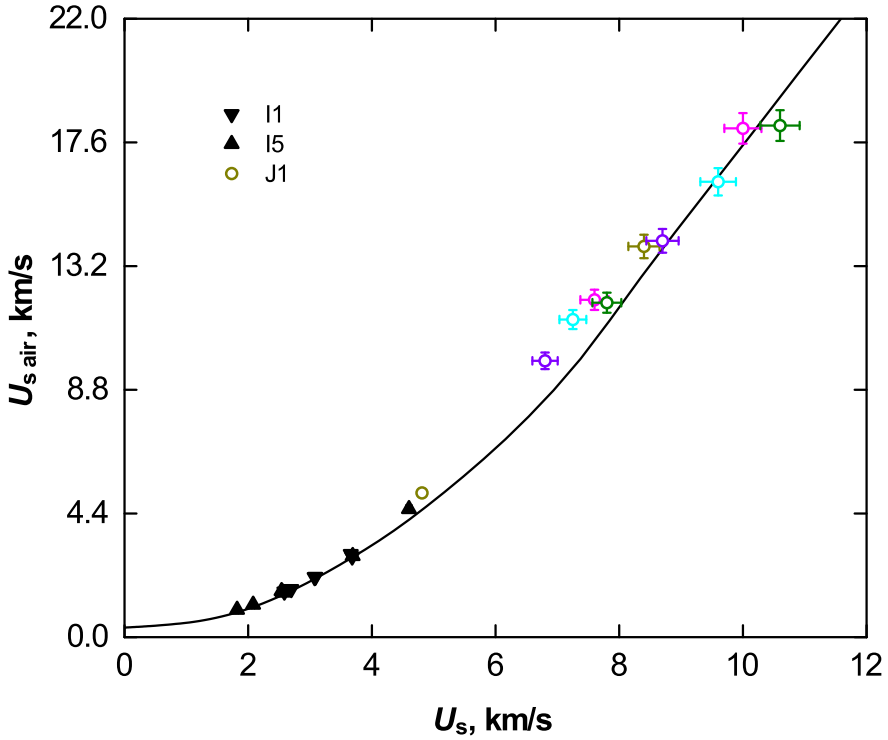

Figure 6. The shock velocity in air ($U_{s\,air}$) as a function of the shock velocity in the bismuth samples (U_s) when the shock front reaches the sample–gas interface: solid line—result of calculation using the present EOS of bismuth and the shock adiabat of air taken from [71]; markers—experimental data (I1—[55]; I5—[59]; J1—[61]).

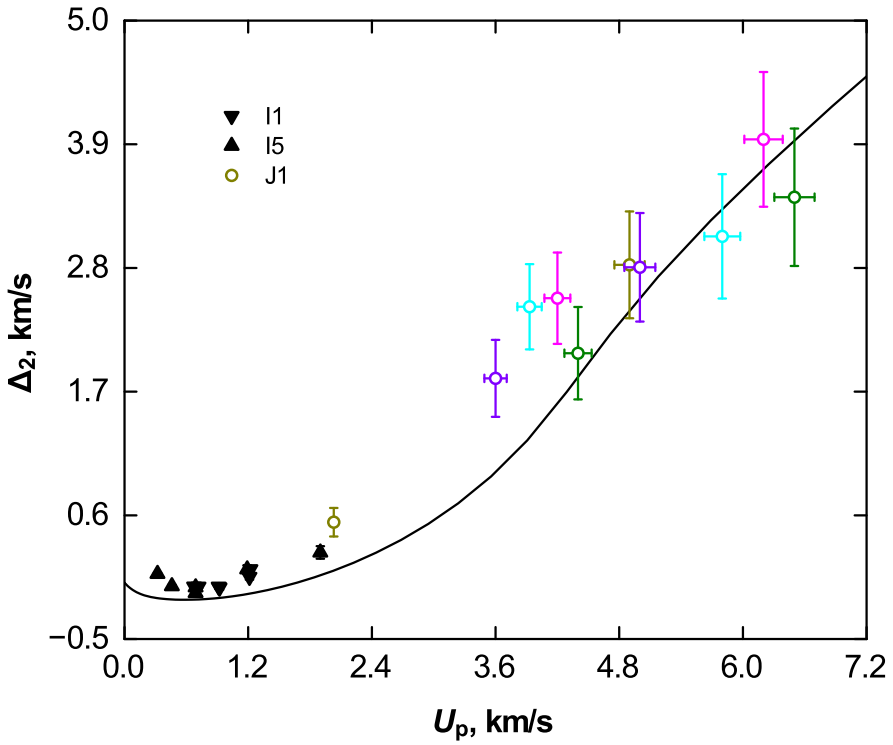

Figure 7. The particle velocity behind the front of the shock wave in air minus twice the particle velocity behind the front of the first shock wave in the bismuth samples ($\Delta_2 = U_{p\,air} - 2U_p$) as a function of U_p; the designations are the same as in Figure 6.

The calculated relationship between the shock velocities in the bismuth samples and in air is shown in Figure 6 in comparison with the experimental points [55,59,61] from Table 1. The agreement of the calculated curve with the data above the velocity $U_s = 7.8$ km/s in bismuth within the experimental error can be seen.

Table 1. Data on isentropic release of shock-compressed bismuth samples into air: U_s, U_p, and P are the shock and particle velocities and the pressure behind the front of the first shock wave in the bismuth samples; $U_{s\,air}$, $U_{p\,air}$, and P_{air} are the shock and particle velocities and the pressure behind the front of the shock wave in air; $\Delta_2 = U_{p\,air} - 2U_p$.

U_s, km/s	U_p, km/s	P, GPa	$U_{s\,air}$, km/s	$U_{p\,air}$, km/s	P_{air}, MPa	Δ_2, km/s
2.696 ± 0.019 [1]	0.718 ± 0.005 [1]	18.95 ± 0.19	1.708 ± 0.011	1.401 ± 0.010 [1]	2.98 ± 0.04	-0.035 ± 0.014
2.585 ± 0.018 [1]	0.676 ± 0.005 [1]	17.11 ± 0.17	1.618 ± 0.010	1.318 ± 0.009 [1]	2.67 ± 0.03	-0.034 ± 0.013
3.075 ± 0.022 [1]	0.914 ± 0.006 [1]	27.52 ± 0.27	2.134 ± 0.014	1.793 ± 0.013 [1]	4.71 ± 0.06	-0.035 ± 0.018
3.084 ± 0.022 [1]	0.922 ± 0.006 [1]	27.84 ± 0.28	2.141 ± 0.014	1.800 ± 0.013 [1]	4.74 ± 0.06	-0.044 ± 0.018
3.682 ± 0.026 [1]	1.212 ± 0.008 [1]	43.69 ± 0.43	2.864 ± 0.018	2.476 ± 0.017 [1]	8.64 ± 0.11	0.052 ± 0.024
3.659 ± 0.026 [1]	1.222 ± 0.009 [1]	43.77 ± 0.43	2.956 ± 0.019	2.564 ± 0.018 [1]	9.23 ± 0.12	0.120 ± 0.025
3.69 ± 0.037 [2]	1.19 ± 0.012 [2]	42.91 ± 0.61	2.889 ± 0.026	2.50 ± 0.025 [2]	8.80 ± 0.17	0.12 ± 0.035
2.56 ± 0.026 [2]	0.69 ± 0.007 [2]	17.27 ± 0.24	1.588 ± 0.014	1.29 ± 0.013 [2]	2.57 ± 0.05	-0.09 ± 0.019
2.54 ± 0.025 [2]	0.69 ± 0.007 [2]	17.14 ± 0.24	1.642 ± 0.015	1.34 ± 0.013 [2]	2.75 ± 0.05	-0.04 ± 0.019
4.60 ± 0.046 [2]	1.90 ± 0.019 [2]	85.6 ± 1.2	4.559 ± 0.044	4.07 ± 0.041 [2]	22.4 ± 0.4	0.27 ± 0.056
2.08 ± 0.021 [2]	0.46 ± 0.005 [2]	9.35 ± 0.13	1.157 ± 0.009	0.89 ± 0.009 [2]	1.34 ± 0.02	-0.03 ± 0.013
1.82 ± 0.018 [2]	0.32 ± 0.003 [2]	5.69 ± 0.11	0.978 ± 0.008	0.72 ± 0.007 [2]	0.95 ± 0.02	0.08 ± 0.010
4.81 ± 0.05 [3]	2.03 ± 0.02 [3]	95.7 ± 1.4	5.13 ± 0.13 [3]	4.60 ± 0.12	28.5 ± 1.5	0.54 ± 0.13
6.80 ± 0.20 [3]	3.60 ± 0.11 [3]	240 ± 10	9.83 ± 0.29 [3]	9.02 ± 0.27	107 ± 6	1.82 ± 0.34
7.25 ± 0.22 [3]	3.93 ± 0.12 [3]	279 ± 12	11.3 ± 0.3 [3]	10.31 ± 0.30	140 ± 8	2.45 ± 0.38
7.6 ± 0.23 [3]	4.2 ± 0.13 [3]	313 ± 13	12.0 ± 0.4 [3]	10.9 ± 0.3	158 ± 9	2.5 ± 0.4
7.8 ± 0.23 [3]	4.4 ± 0.13 [3]	336 ± 14	11.9 ± 0.4 [3]	10.8 ± 0.3	155 ± 9	2.0 ± 0.4
8.4 ± 0.25 [3]	4.9 ± 0.15 [3]	403 ± 17	13.9 ± 0.4 [3]	12.6 ± 0.4	211 ± 13	2.8 ± 0.5
8.7 ± 0.26 [3]	5.0 ± 0.15 [3]	426 ± 18	14.1 ± 0.4 [3]	12.8 ± 0.4	218 ± 13	2.8 ± 0.5
9.6 ± 0.29 [3]	5.8 ± 0.17 [3]	546 ± 23	16.2 ± 0.5 [3]	14.7 ± 0.4	286 ± 17	3.1 ± 0.6
10.0 ± 0.3 [3]	6.2 ± 0.19 [3]	608 ± 26	18.1 ± 0.5 [3]	16.3 ± 0.5	356 ± 21	3.9 ± 0.6
10.6 ± 0.3 [3]	6.5 ± 0.20 [3]	675 ± 29	18.2 ± 0.5 [3]	16.4 ± 0.5	360 ± 21	3.4 ± 0.6

[1] Values taken from [55]. [2] Values taken from [59]. [3] Values taken from [61].

It seems interesting to evaluate the deviation from the rule of doubling the velocity of matter during the isentropic expansion of a shock-compressed sample into air [72,73] for bismuth. The calculated dependence of the particle velocity of shock-compressed air ($U_{p\,air}$) minus the double mass velocity of shock-compressed bismuth (U_p) on the latter is shown in Figure 7 in comparison with the experimental points [55,59,61] from Table 1. As can be seen in Figure 7, this calculated dependence agrees with the data within the experimental error at particle velocities in bismuth above $U_p = 4.4$ km/s.

4. Conclusions

Thus, the proposed EOS model as a function of pressure on the specific volume and specific internal energy is applicable for generalizing the available experimental and theoretical information about the properties of a substance in a wide range of thermodynamic parameters. The newly constructed EOS for the bcc and liquid phases of bismuth is in good agreement with the available experimental data, with the exception of the region of relatively low pressures achieved at low expansion velocities of the shock-compressed material into barriers with low dynamic impedance, where phase transitions (melting, evaporation) occur. The refined parameters of shock waves in air under the experimental conditions on the isentropic expansion of shock-compressed bismuth samples provide additional information that can be applied to the study of phase transitions in this metal. The developed EOS can be effectively used in numerical simulations of various processes in bismuth at high energy densities.

Funding: This research was supported by the Ministry of Science and Higher Education of the Russian Federation (agreement with the Joint Institute for High Temperatures RAS No. 075-15-2020-785 dated 23 September 2020).

Institutional Review Board Statement: Not applicable.

Informed Consent Statement: Not applicable.

Data Availability Statement: The data presented in this study are available from the author upon reasonable request.

Conflicts of Interest: The author declares no conflict of interest.

References

1. Zel'dovich, Y.B.; Raizer, Y.P. *Physics of Shock Waves and High-Temperature Hydrodynamic Phenomena*; Academic Press: New York, NY, USA, 1967.
2. Bushman, A.V.; Fortov, V.E.; Kanel', G.I.; Ni, A.L. *Intense Dynamic Loading of Condensed Matter*; Taylor & Francis: Washington, DC, USA, 1993.
3. Fortov, V.E. *Extreme States of Matter: High Energy Density Physics*, 2nd ed.; Springer Series in Materials Science; Springer: Berlin/Heidelberg, Germany, 2016; Volume 216.
4. Aleksandrov, V.V.; Branitskii, A.V.; Grabovski, E.V.; Laukhin, Y.N.; Oleinik, G.M.; Tkachenko, S.I.; Frolov, I.N.; Khishchenko, K.V. Study of the impact of a duralumin flyer with a tungsten target at the Angara-5-1 facility. *Plasma Phys. Rep.* **2019**, *45*, 421–426. [CrossRef]
5. Kraus, E.I.; Fomin, V.M.; Shabalin, I.I. Construction of a unified curve in modeling the process of crater formation by compact projectiles of different shapes. *J. Appl. Mech. Tech. Phys.* **2020**, *61*, 855–865. [CrossRef]
6. Rodionov, E.S.; Lupanov, V.G.; Gracheva, N.A.; Mayer, P.N.; Mayer, A.E. Taylor impact tests with copper cylinders: Experiments, microstructural analysis and 3D SPH modeling with dislocation plasticity and MD-informed artificial neural network as equation of state. *Metals* **2022**, *12*, 264. [CrossRef]
7. Lapushkina, T. Principles of magnetohydrodynamical control of internal and external supersonic flows. *Energies* **2022**, *15*, 5641. [CrossRef]
8. Ashitkov, S.I.; Komarov, P.S.; Struleva, E.V.; Agranat, M.B.; Kanel, G.I.; Khishchenko, K.V. The behavior of tantalum under ultrashort loads induced by femtosecond laser. *J. Phys. Conf. Ser.* **2015**, *653*, 012001. [CrossRef]
9. Tan, S.; Wang, M.; Wu, J.; Zhang, Y.; Li, J. A study on the plasma plume expansion dynamics of nanosecond laser ablating Al/PTFE. *Energies* **2020**, *13*, 3321. [CrossRef]
10. Semenov, A.Y.; Stuchebryukhov, I.A.; Khishchenko, K.V. Modeling of shock-wave processes in aluminum under the action of a short laser pulse. *Math. Montis.* **2021**, *50*, 108–118. [CrossRef]
11. Khokhlov, V.A.; Zhakhovsky, V.V.; Inogamov, N.A.; Ashitkov, S.I.; Sitnikov, D.S.; Khishchenko, K.V.; Petrov, Y.V.; Manokhin, S.S.; Nelasov, I.V.; Shepelev, V.V.; et al. Melting of titanium by a shock wave generated by an intense femtosecond laser pulse. *JETP Lett.* **2022**, *115*, 523–530.
12. Gnyusov, S.F.; Rotshtein, V.P.; Mayer, A.E.; Rostov, V.V.; Gunin, A.V.; Khishchenko, K.V.; Levashov, P.R. Simulation and experimental investigation of the spall fracture of 304L stainless steel irradiated by a nanosecond relativistic high-current electron beam. *Int. J. Fract.* **2016**, *199*, 59–70.
13. Khishchenko, K.V.; Charakhch'yan, A.A. Reflection of detonation wave from the symmetry plane within a cylindrical target for controlled thermonuclear fusion. *Comput. Math. Math. Phys.* **2021**, *61*, 1682–1699. [CrossRef]
14. Sadovnichii, D.N.; Milekhin, Y.M.; Kalinin, Y.G.; Kazakov, E.D.; Lavrov, G.S.; Sheremet'ev, K.Y. Impact of a relativistic electron beam on cast aluminized energetic condensed systems. *Combust. Explos. Shock Waves* **2022**, *58*, 206–216. [CrossRef]
15. Kondratyev, A.M.; Korobenko, V.N.; Rakhel, A.D. Metal–non-metal transition in lead–bismuth eutectic. *J. Phys. Condens. Matter* **2022**, *34*, 195601. [CrossRef]
16. Maler, D.; Efimov, S.; Liverts, M.; Theocharous, S.; Strucka, J.; Yao, Y.; Proud, W.; Rack, A.; Lukic, B.; Bland, S.N.; et al. Peculiarities of planar shockwave interaction with air–water interface and solid target. *Phys. Plasmas* **2022**, *29*, 063502. [CrossRef]
17. Barengolts, S.A.; Uimanov, I.V.; Oreshkin, V.I.; Khishchenko, K.V.; Oreshkin, E.V. Effect of the temperature of an electrode microprotrusion on the microcrater formation on the electrode surface upon pulsed and radiofrequency vacuum breakdowns. *Vacuum* **2022**, *204*, 111364. [CrossRef]
18. Lomonosov, I.V.; Fortova, S.V. Wide-range semiempirical equations of state of matter for numerical simulation on high-energy processes. *High Temp.* **2017**, *55*, 585–610. [CrossRef]
19. Azarova, O.A.; Lapushkina, T.A.; Krasnobaev, K.V.; Kravchenko, O.V. Redistribution of energy during interaction of a shock wave with a temperature layered plasma region at hypersonic speeds. *Aerospace* **2021**, *8*, 326. [CrossRef]
20. Mursenkova, I.V.; Ivanov, I.E.; Liao, Y.; Kryukov, I.A. Experimental and numerical investigation of a surface sliding discharge in a supersonic flow with an oblique shock wave. *Energies* **2022**, *15*, 2189. [CrossRef]
21. Li, Y.; Shen, S.; Niu, C.; Guo, Y.; Zhang, L. The effect of different pressure conditions on shock waves in a supersonic steam ejector. *Energies* **2022**, *15*, 2903. [CrossRef]

22. Cai, F.; Huang, G.; Liu, X. Investigation of shock wave oscillation suppression by overflow in the supersonic inlet. *Energies* **2022**, *15*, 3879. [CrossRef]
23. Sokolova, T.S.; Dorogokupets, P.I. Equations of state of Ca-silicates and phase diagram of the $CaSiO_3$ system under upper mantle conditions. *Minerals* **2021**, *11*, 322. [CrossRef]
24. Liu, Y.; Zhang, X.; Bi, H.; Liu, X.; Wang, F. First-principles prediction of structure, mechanical and thermodynamic properties of $Bi_xGe_yO_z$ ternary bismuth crystals. *Vacuum* **2022**, *195*, 110696. [CrossRef]
25. Li, Y.; Sun, S.; He, Y.; Li, H. First-principles calculations about elastic and Li^+ transport properties of lithium superoxides under high pressure and high temperature. *Chin. Phys. Lett.* **2021**, *39*, 026101. [CrossRef]
26. Sokolova, T.S.; Dorogokupets, P.I.; Filippova, A.I. Equations of state of clino- and orthoenstatite and phase relations in the $MgSiO_3$ system at pressures up to 12 GPa and high temperatures. *Phys. Chem. Miner.* **2022**, *49*, 37. [CrossRef]
27. Horsley, G.W. The preparation of bismuth for use in a liquid-metal fuelled reactor. *J. Nucl. Energy* **1957**, *6*, 41–52. [CrossRef]
28. Bauer, G.S.; Salvatores, M.; Heusener, G. MEGAPIE, a 1 MW pilot experiment for a liquid metal spallation target. *J. Nucl. Mater.* **2001**, *296*, 17–33. [CrossRef]
29. Borella, A.; Belgya, T.; Kopecky, S.; Gunsing, F.; Moxon, M.; Rejmund, M.; Schillebeeckx, P.; Szentmiklosi, L. Determination of the $^{209}Bi(n,\gamma)^{210}Bi$ and $^{209}Bi(n,\gamma)^{210m,g}Bi$ reaction cross sections in a cold neutron beam. *Nucl. Phys. A* **2011**, *850*, 1–21. [CrossRef]
30. Mueller, A.C. Transmutation of nuclear waste and the future MYRRHA demonstrator. *J. Phys. Conf. Ser.* **2013**, *420*, 012059. [CrossRef]
31. Shor, A.; Weissman, L.; Tessler, M.; Aviv, O.; Eisen, Y.; Feinberg, G.; Mishnayot, Y.; Plompen, A.; Vaintraub, S. Measurements of the ^{210g}Bi to ^{210m}Bi activation ratio for the $^{209}Bi(n,\gamma)$ reaction with thermal and epithermal neutrons at the Soreq IRR1 reactor. *Phys. Rev. C* **2022**, *105*, 025802. [CrossRef]
32. Johnson, J.N.; Hayes, D.B.; Asay, J.R. Equations of state and shock-induced transformations in solid I–solid II–liquid bismuth. *J. Phys. Chem. Solids* **1974**, *35*, 501–515. [CrossRef]
33. Bushman, A.V.; Glushak, B.L.; Gryaznov, V.K.; Zhernokletov, M.V.; Krasyuk, I.K.; Pashinin, P.P.; Prokhorov, A.M.; Ternovoi, V.Y.; Filimonov, A.S.; Fortov, V.E. Shock compression and adiabatic decompression of a dense bismuth plasma at extreme thermal energy densities. *JETP Lett.* **1986**, *44*, 480–483.
34. Lomonosov, I.V.; Fortov, V.E.; Khishchenko, K.V.; Levashov, P.R. Phase diagrams and thermodynamic properties of metals at high pressures, high temperatures. *AIP Conf. Proc.* **2002**, *620*, 111–114.
35. Heuze, O. Building of equations of state with numerous phase transitions—Application to bismuth. *AIP Conf. Proc.* **2006**, *845*, 212–215.
36. Kane, J.O.; Smith, R.F. Modeling non-equilibrium phase transitions in isentropically compressed Bi. *AIP Conf. Proc.* **2006**, *845*, 244–247.
37. Cox, G.A. A multi-phase equation of state for bismuth. *AIP Conf. Proc.* **2007**, *955*, 151–154.
38. Li, Y.H.; Chang, J.Z.; Li, X.M.; Yu, Y.Y.; Dai, C.D.; Zhang, L. Multiphase equation of states of solid and liquid phases for bismuth. *Acta Phys. Sin.* **2012**, *61*, 206203.
39. Fortov, V.E.; Lomonosov, I.V. Ya B Zeldovich and equation of state problems for matter under extreme conditions. *Phys. Usp.* **2014**, *57*, 219–233. [CrossRef]
40. Kinelovskii, S.A.; Maevskii, K.K. Modeling shock loading of multicomponent materials including bismuth. *High Temp.* **2016**, *54*, 675–681. [CrossRef]
41. Su, C.; Liu, Y.; Wang, Z.; Song, W.; Asimow, P.D.; Tang, H.; Xie, H. Equation of state of liquid bismuth and its melting curve from ultrasonic investigation at high pressure. *Phys. B* **2017**, *524*, 154–162. [CrossRef]
42. Kirzhnits, D.A. Quantum corrections to the Thomas–Fermi equation. *Sov. Phys. JETP* **1957**, *5*, 64–71.
43. Kirzhnits, D.A. The limits of applicability of the quasi-classical equation of state of matter. *Sov. Phys. JETP* **1959**, *8*, 1081–1089.
44. Kalitkin, N.N. The Thomas–Fermi model of the atom with quantum and exchange corrections. *Sov. Phys. JETP* **1960**, *11*, 1106–1110.
45. Kalitkin, N.N.; Kuzmina, L.V. *Tables of Thermodynamic Functions of Matter at High Concentration of Energy*; Institute of Applied Mathematics of the Academy of Sciences USSR: Moscow, Russia, 1975.
46. Khishchenko, K.V. The equation of state for magnesium at high pressures. *Tech. Phys. Lett.* **2004**, *30*, 829–831. [CrossRef]
47. Lomonosov, I.V.; Fortov, V.E.; Khishchenko, K.V. Model of wide-range equations of polymer materials state under high-energy densities. *Khim. Fiz.* **1995**, *14*, 47–52.
48. Bushman, A.V.; Zhernokletov, M.V.; Lomonosov, I.V.; Sutulov, Y.N.; Fortov, V.E.; Khishchenko, K.V. Experimental study of phenylone and polystyrene under the shock loading conditions and isentropic expansion. Plastics state equation under high densities of energy. *Zh. Eksp. Teor. Fiz.* **1996**, *109*, 1662–1670.
49. Tonkov, E.Y. *Phase Diagrams of Elements at High Pressures*; Nauka: Moscow, Russia, 1979.
50. Decker, D.L.; Bassett, W.A.; Merrill, L.; Hall, H.T.; Barnett, J.D. High-pressure calibration: A critical review. *J. Phys. Chem. Ref. Data* **1972**, *1*, 773–835. [CrossRef]
51. McMahon, M.I.; Degtyareva, O.; Nelmes, R.J. Ba-IV-type incommensurate crystal structure in group-V metals. *Phys. Rev. Lett.* **2000**, *85*, 4896–4899. [CrossRef]
52. Degtyareva, O.; McMahon, M.I.; Nelmes, R.J. High-pressure structural studies of group-15 elements. *High Press. Res.* **2004**, *24*, 319–356. [CrossRef]

53. Akahama, Y.; Kawamura, H.; Singh, A.K. Equation of state of bismuth to 222 GPa and comparison of gold and platinum pressure scales to 145 GPa. *J. Appl. Phys.* **2002**, *92*, 5892–5897. [CrossRef]
54. Akahama, Y.; Kawamura, H.; Singh, A.K. The equation of state of Bi and cross-checking of Au and Pt scales to megabar pressure. *J. Phys. Condens. Matter* **2002**, *14*, 11495–11500. [CrossRef]
55. Walsh, J.M.; Rice, M.H.; McQueen, R.G.; Yarger, F.L. Shock-wave compressions of twenty-seven metals. Equations of state of metals. *Phys. Rev.* **1957**, *108*, 196–216. [CrossRef]
56. Al'tshuler, L.V.; Krupnikov, K.K.; Brazhnik, M.I. Dynamic compressibility of metals under pressure from 400,000 to 4,000,000 atmospheres. *Sov. Phys. JETP* **1958**, *7*, 614–619.
57. McQueen, R.G.; Marsh, S.P. Equation of state for nineteen metallic elements from shock-wave measurements to two megabars. *J. Appl. Phys.* **1960**, *31*, 1253–1269. [CrossRef]
58. Romain, J.P. Phase transformation in bismuth under shock loading. *J. Appl. Phys.* **1974**, *45*, 135–139. [CrossRef]
59. van Thiel, M. *Compendium of Shock-Wave Data*; Report UCRL-50108; Lawrence Livermore Laboratory: Livermore, CA, USA, 1977.
60. Marsh, S.P. (Ed.) *LASL Shock Hugoniot Data*; University of California Press: Berkeley, CA, USA, 1980.
61. Glushak, B.L.; Zharkov, A.P.; Zhernokletov, M.V.; Ternovoi, V.Y.; Filimonov, A.S.; Fortov, V.E. Experimental investigation of the thermodynamics of dense plasmas formed from metals at high energy concentrations. *Sov. Phys. JETP* **1989**, *69*, 739–749.
62. Trunin, R.F.; Zhernokletov, M.V.; Kuznetsov, N.F.; Shutov, V.V. Dynamic compressibility of molten and cooled metals. *High Temp.* **1995**, *33*, 220–224.
63. Podurets, A.M.; Dorokhin, V.V.; Trunin, R.F. X-ray diffraction study of shock-induced phase transformations in zirconium and bismuth. *High Temp.* **2003**, *41*, 216–220. [CrossRef]
64. Tan, Y.; Yu, Y.; Dai, C.; Jin, K.; Wang, Q.; Hu, J.; Tan, H. Hugoniot and sound velocity measurements of bismuth in the range of 11–70 GPa. *J. Appl. Phys.* **2013**, *113*, 093509. [CrossRef]
65. Li, X.M.; Yu, Y.Y.; Tan, Y.; Hu, C.M.; Zhang, Z.G.; Lan, Q.; Fu, Q.W.; Jing, H.H. Softening of sound velocity and Hugoniot parameter measurement for shocked bismuth in the solid–liquid mixing pressure zone. *Acta Phys. Sin.* **2018**, *67*, 046401.
66. Xi, F.; Jin, K.; Geng, H.; Li, Y.; Tan, Y.; Li, J.; Zhang, Y.; Zhang, L.; Cai, L.; Sun, Y. Accurate Hugoniots and sound velocities of bismuth under shock compression in the 38–100 GPa range. *AIP Adv.* **2018**, *8*, 015023. [CrossRef]
67. Gorman, M.G.; Coleman, A.L.; Briggs, R.; McWilliams, R.S.; McGonegle, D.; Bolme, C.A.; Gleason, A.E.; Galtier, E.; Lee, H.J.; Granados, E.; et al. Femtosecond diffraction studies of solid and liquid phase changes in shock-compressed bismuth. *Sci. Rep.* **2018**, *8*, 16927. [CrossRef]
68. Balandina, A.N.; Burnashov, V.A.; Voronin, A.V.; Kalinkin, S.Y.; Mikhailov, A.L.; Podurets, A.M.; Simakov, V.G.; Tereshkina, I.A.; Tkachenko, M.I.; Trunin, I.R.; et al. Microstructure of shocked preheated bismuth and detection of melting at pressures of 1.6–2.4 GPa. *Combust. Explos. Shock Waves* **2018**, *54*, 535–542. [CrossRef]
69. Al'tshuler, L.V.; Trunin, R.F.; Krupnikov, K.K.; Panov, N.V. Explosive laboratory devices for shock wave compression studies. *Usp. Fiz. Nauk* **1996**, *166*, 575–581. [CrossRef]
70. Funtikov, A.I. Explosive laboratory measurement of the dynamical compressibility of porous substances in the pressure range from 0.1 to 1 TPa. *Usp. Fiz. Nauk* **1997**, *167*, 1119–1120. [CrossRef]
71. Kuznetsov, N.N. *Thermodynamic Functions and Shock Adiabats of Air at High Temperatures*; Mashinostroyeniye: Moscow, Russia, 1965.
72. Al'tshuler, L.V.; Bakanova, A.A.; Bushman, A.V.; Dudoladov, I.P.; Zubarev, V.N. Evaporation of shock compressed lead in release waves. *Zh. Eksp. Teor. Fiz.* **1977**, *73*, 1866–1872.
73. Zhernokletov, M.V.; Simakov, G.V.; Sutulov, Y.N.; Trunin, R.F. Expansion isentropes of aluminum, iron, molybdenum, lead, and tantalum. *High Temp.* **1995**, *33*, 36–39.